

Bandgaps of insulators from moment-functional based spectral density-functional theory

Frank Freimuth^{1,2,*}, Stefan Blügel¹, and Yuriy Mokrousov^{1,2}

¹*Peter Grünberg Institut and Institute for Advanced Simulation,*

Forschungszentrum Jülich and JARA, 52425 Jülich, Germany and

²*Institute of Physics, Johannes Gutenberg University Mainz, 55099 Mainz, Germany*

Within the method of spectral moments it is possible to construct the spectral function of a many-electron system from the first $2P$ spectral moments ($P = 1, 2, 3, \dots$). The case $P = 1$ corresponds to standard Kohn-Sham density functional theory (KS-DFT). Taking $P > 1$ allows us to consider additional important properties of the uniform electron gas (UEG) in the construction of suitable moment potentials for moment-functional based spectral density-functional theory (MFbSDFT). For example, the quasiparticle renormalization factor Z , which is not explicitly considered in KS-DFT, can be included easily. In the 4-pole approximation of the spectral function of the UEG (corresponding to $P = 4$) we can reproduce the momentum distribution, the second spectral moment, and the charge response acceptably well, while a treatment of the UEG by KS-DFT reproduces from these properties only the charge response. For weakly and moderately correlated systems we may reproduce the most important aspects of the 4-pole approximation by an optimized two-pole model, which leaves away the low-energy satellite band. From the optimized two-pole model we extract *parameter-free universal* moment potentials for MFbSDFT, which improve the description of the bandgaps in Si, SiC, BN, MgO, CaO, and ZnO significantly.

I. INTRODUCTION

Density functionals for KS-DFT are often constructed from the exchange-correlation energy of the UEG [1, 2]. Several other important properties of the UEG, such as the quasiparticle renormalization factor Z [3], the effective mass m^* , the Landau liquid parameters, the momentum distribution function n_k [4], and the spectral moments [5] are not built-in explicitly into KS-DFT. In particular, KS-DFT uses $Z = 1$ by construction. In order to obtain realistic Z factors KS-DFT may be combined with many-body techniques such as DMFT [6, 7]. Within DMFT the effective mass enhancement is correlated with the inverse quasiparticle renormalization factor, i.e., $m^*/m = Z^{-1}$ [8], and consequently DMFT predicts many-body corrections of this quantity as well.

There are several reasons why standard KS-DFT uses only the exchange-correlation energy of the UEG explicitly, while not employing additionally any other of its many well-studied properties directly. The most important reason is that the Hohenberg-Kohn theorem establishes a direct relation between the exchange-correlation energy of the UEG and the one of the real solid studied by KS-DFT [9, 10], while such relations have either not been suggested for other properties of the UEG, or, in case they have been suggested, their validity is still under debate or the exact form of the relation is unknown. For example, several works suggested that the bandnarrowing found in experiments and calculations of the Alkali metals [11] can be explained by a bandnarrowing found in earlier theories of the UEG [12]. However, recent work [3] finds the bandnarrowing in the UEG to be much smaller than in the earlier calculations, which suggests that for this quantity there might not be a useful relation between

the UEG and realistic materials.

On the other hand, it seems plausible that the Z renormalization factor of quasiparticles at the Fermi surface of a realistic material might be related to its counterpart in the UEG. One reason why Z cannot be included explicitly into standard KS-DFT is that only one effective potential is used there, which only takes into account the lattice potential, the Coulomb potential, and the exchange-correlation potential.

Recently, we have suggested a moment-functional based spectral-density functional theory (MFbSDFT) [13], which computes the spectral function matrix $S_{nm}(E)$ from its spectral moment matrices

$$M_{nm}^{(I)} = \frac{1}{\hbar} \int dE E^I S_{nm}(E), \quad (1)$$

where $I = 1, 2, 3, \dots$. The key assumption of this approach is that the spectral moment matrices $M_{nm}^{(I)}$ can be computed from the KS-Hamiltonian without correlation, i.e., only with the local exchange, and additional correction terms $M_{nm}^{(I+)}$, which can be obtained from moment potentials $\mathcal{V}^{(I+)}(\mathbf{r})$:

$$M_{nm}^{(I+)} = \int d^3r \mathcal{V}^{(I+)}(\mathbf{r}) [\phi_n(\mathbf{r})]^* \phi_m(\mathbf{r}), \quad (2)$$

where $\phi_n(\mathbf{r})$ are orthonormalized basis functions. We have suggested [13] that these moment potentials $\mathcal{V}^{(I+)}(\mathbf{r})$ are likely to be given by universal functionals of the charge density, similar to the exchange correlation functional.

In practical calculations one will have to choose the maximal I in Eq. (1), i.e., one will choose $I \leq 3$, or $I \leq 5$, or $I \leq 7$, or $I \leq 9, \dots$. By increasing the maximum I one increases the precision of MFbSDFT. By

increasing the maximum I one may also employ more and more properties of the UEG through the additional moment potentials. For example $I \leq 1$ requires $Z = 1$, but already with $I \leq 3$ it is possible to impose $Z \leq 1$. However, the moment potentials $\mathcal{V}^{(I+)}(\mathbf{r})$ with high I are still unknown. For $I = 1$ and $I = 2$ they may be obtained from models of the spectral moments of the UEG [5].

In Ref. [14] we have suggested to compute $M_{nm}^{(3+)}$ from the momentum distribution function n_k of the UEG when the second moment correction $M_{nm}^{(2+)}$ is known. We have shown that this may improve the spectra in comparison to standard KS-DFT in some cases. In Ref. [14] we considered n_k only in the vicinity of the Fermi surface. In the present work we refine the approach of Ref. [14] further, notably we pay attention to the normalization of n_k and to its integral up to the Fermi wave number k_F . We show that these properties of the UEG can be reproduced when it is modelled within the 4-pole approximation. Since the quasiparticle renormalization factor Z in the UEG is related to the discontinuity of n_k at k_F [15], our 4-pole model also includes Z by construction. Our 4-pole model may be used to obtain moment potentials for $I \leq 7$.

There are many cases where KS-DFT does not predict the spectral properties satisfactorily. Notably, the bandgap in insulators deviates often substantially from experiment [16]. In strongly correlated materials the upper and lower Hubbard bands may be missing in the KS-spectrum [17, 18]. Even in simple metals such as Na and K the bandwidths may differ significantly from experiment [11]. To improve all these spectral properties by MFbSDFT might be possible, but this would require a sufficient number of moment potentials $\mathcal{V}^{(I+)}(\mathbf{r})$ with sufficient accuracy, which are not available yet.

However, bandgaps can often be corrected by LDA+ U , while missing upper or lower Hubbard bands or wrong bandwidths often cannot be corrected easily by LDA+ U . Correcting the bandgap may therefore define a goal that can be achieved by MFbSDFT with a minimum number of moment potentials. If universal moment potentials can be found that correct the bandgap in many insulators, it corroborates the key assumptions of the MFbSDFT approach. We show in this work that this is indeed the case: Already the moments with $I \leq 3$ are sufficient to correct the bandgap in many insulators. This provides a strong motivation to develop suitable models also for the higher spectral moments of the UEG in order to reproduce additionally the experimental bandwidths and upper and lower Hubbard bands in future improvements of the MFbSDFT method.

The rest of this paper is structured as follows: In Sec. II A we explain how higher spectral moments may be expressed in terms of lower spectral moments and additional correction terms. Additionally, we introduce the zero-bandnarrowing approximation of the UEG. In Sec. II B and in Sec. II C we discuss in detail the three-

pole and four-pole approximations of the UEG, respectively. In Sec. II D we describe an $(n+1)$ -pole approximation of the UEG, which further improves the description in particular of n_k . In Sec. II E we explain how the two-pole approximation can be optimized for weakly and moderately correlated systems by leaving away the low-energy satellite band. In Sec. III we present the results of first-principles MFbSDFT calculations based on the moment potentials obtained from these models of the UEG. This paper ends with a summary in Sec. IV. In the Appendices we discuss how to obtain $M^{(2+)}$ from the model developed in Ref. [5] (Sec. A) and how to compute the spectral function from the first 6 spectral moments (Sec. B).

II. THEORY

A. Expressing spectral moments in terms of lower spectral moments and correction terms

The matrix elements of the spectral moment $\mathbf{M}^{(1)}$ are given by [13]

$$M_{nm}^{(1)} = T_{nm} + V_{nm}^H + V_{nm}^X, \quad (3)$$

where

$$T_{nm} = \int d^3r \phi_n^*(\mathbf{r}) \left[-\frac{\hbar^2}{2m} \Delta + V(\mathbf{r}) \right] \phi_m(\mathbf{r}) \quad (4)$$

comprises the kinetic energy and the crystal potential $V(\mathbf{r})$, V_{nm}^H are the matrix elements of the Hartree potential, and

$$V_{nm}^X = -\frac{\hbar^2}{ma_B^2} \left[\frac{3}{2\pi} \right]^{\frac{2}{3}} \int d^3r \phi_n^*(\mathbf{r}) \phi_m(\mathbf{r}) \frac{1}{r_s(\mathbf{r})} \quad (5)$$

are the matrix elements of the local exchange potential, where

$$r_s(\mathbf{r}) = \frac{1}{a_B} \left(\frac{3}{4\pi n_e(\mathbf{r})} \right)^{\frac{1}{3}} \quad (6)$$

is the dimensionless density parameter [15], and a_B is the Bohr radius. r_s depends on the position \mathbf{r} through the electron density $n_e(\mathbf{r})$.

We express the second moment matrix $\mathbf{M}^{(2)}$ in terms of the square of the first moment matrix $\mathbf{M}^{(1)}$ and the correction term $\mathbf{M}^{(2+)}$ [13]:

$$\mathbf{M}^{(2)} = \left[\mathbf{M}^{(1)} \right]^2 + \mathbf{M}^{(2+)}. \quad (7)$$

The correction term $\mathbf{M}^{(2+)}$ may be computed from the moment potential $\mathcal{V}^{(2+)}$ according to Eq. (2). A model for $\mathcal{V}^{(2+)}$, which has been derived from the spectral moments of the UEG, is described in the Appendix A.

In Ref. [13] we suggested to use

$$\mathbf{M}^{(3)} = [\mathbf{M}^{(1)}]^3 + \mathbf{M}^{(3+)} \quad (8)$$

and we have shown that the spectra can be improved in some cases using this expression. However, Eq. (8) is not the only possible form that one may suggest. For example

$$\mathbf{M}^{(3)} = \frac{1}{2} \mathbf{M}^{(1)} \mathbf{M}^{(2)} + \frac{1}{2} \mathbf{M}^{(2)} \mathbf{M}^{(1)} + \mathbf{M}^{(3+)} \quad (9)$$

is a priori also a possible form. When we describe the UEG with the method of spectral moments and set $M^{(2+)}$ and $M^{(3+)}$ to k -independent constants (in the UEG the $M^{(I+)}$ are real-valued numbers and not matrices, therefore we do not use bold-face when $M^{(I+)}$ or $M^{(I)}$ refer to the UEG) we find that e.g. the bandnarrowing may differ depending on whether Eq. (8) or Eq. (9) is used. If we used a k -dependent $M^{(3+)}$ we could obviously obtain the same results from both Eq. (8) and Eq. (9) (clearly, the $M^{(3+)}$ to be used together with Eq. (8) would differ from the $M^{(3+)}$ to be used together with Eq. (9)). However, when we choose $M^{(3+)}$ to be independent of k the question arises of whether Eq. (8) or Eq. (9) is the better alternative.

More generally, we might even consider

$$\begin{aligned} \mathbf{M}^{(3)} = & \frac{\gamma}{2} \mathbf{M}^{(1)} \mathbf{M}^{(2)} + \frac{\gamma}{2} \mathbf{M}^{(2)} \mathbf{M}^{(1)} \\ & + (1 - \gamma) [\mathbf{M}^{(1)}]^3 + \mathbf{M}^{(3+)} \end{aligned} \quad (10)$$

with a parameter γ that could be chosen to optimize the results. For example, one might determine γ so that the bandnarrowing of the UEG is reproduced as well as possible by the method of spectral moments with k -independent $M^{(I+)}$.

At $r_s = 4$ the bandnarrowing in the UEG is only 4-7% according to the variational diagrammatic Monte Carlo calculations of Ref. [3]. However, values of the bandnarrowing for the full range of variation of r_s (see Table I) as used in first-principles calculations have not yet been published for the variational diagrammatic Monte Carlo method. For small bandnarrowings that do not exceed 4-7% it is plausible that a zero-bandnarrowing approximation of the UEG may yield useful results. It will become clear in Sec. II B, Sec. II C, and Sec. II D that it is indeed very instructive and insightful to develop and to investigate such a zero-bandnarrowing approximation of the UEG.

Interestingly, it is rather easy to determine the coefficient γ in Eq. (10) so that the bandnarrowing is precisely zero. The basic observation is that we may rewrite Eq. (7) as follows:

$$\begin{aligned} \mathbf{M}^{(2+)} = & \mathbf{M}^{(2)} - [\mathbf{M}^{(1)}]^2 = \\ = & \frac{1}{\hbar} \int [E - \mathbf{M}^{(1)}]^2 \mathbf{S}(E) dE. \end{aligned} \quad (11)$$

Generalizing this expression to $I = 3$ we obtain

$$\begin{aligned} \mathbf{M}^{(3+)} = & \frac{1}{\hbar} \text{Re} \left\{ \int [E - \mathbf{M}^{(1)}]^3 \mathbf{S}(E) dE \right\} = \\ = & \mathbf{M}^{(3)} + 2 [\mathbf{M}^{(1)}]^3 - \frac{3}{2} [\mathbf{M}^{(2)} \mathbf{M}^{(1)} + \mathbf{M}^{(1)} \mathbf{M}^{(2)}], \end{aligned} \quad (12)$$

where we define the real-part of a matrix \mathbf{A} as

$$\text{Re} \mathbf{A} = \frac{1}{2} [\mathbf{A} + \mathbf{A}^\dagger]. \quad (13)$$

Using Eq. (13) ensures that the spectral moment correction is hermitian. Comparing Eq. (12) to Eq. (10) we find that they become equivalent when we set $\gamma = 3$. In practice, $\mathbf{M}^{(2+)}$ and $\mathbf{M}^{(3+)}$ are computed from suitable moment potentials according to Eq. (2). Next, one computes $\mathbf{M}^{(2)}$ from Eq. (7). Finally, one computes $\mathbf{M}^{(3)}$ from Eq. (12). When one uses this recipe to compute the bandstructure of the UEG one finds that the bandnarrowing is zero.

This recipe produces also a zero bandnarrowing in the UEG when we include more moments. For $I = 4$ we have

$$\begin{aligned} \mathbf{M}^{(4+)} = & \frac{1}{\hbar} \text{Re} \left[\int [E - \mathbf{M}^{(1)}]^4 \mathbf{S}(E) dE \right] = \mathbf{M}^{(4)} \\ - & 4 \text{Re} [\mathbf{M}^{(3)} \mathbf{M}^{(1)}] + 6 \text{Re} [\mathbf{M}^{(2)} [\mathbf{M}^{(1)}]^2] - 3 [\mathbf{M}^{(1)}]^4 \end{aligned} \quad (14)$$

and for $I = 5$ we have

$$\begin{aligned} \mathbf{M}^{(5+)} = & \frac{1}{\hbar} \text{Re} \left[\int [E - \mathbf{M}^{(1)}]^5 \mathbf{S}(E) dE \right] = \mathbf{M}^{(5)} \\ - & 10 \text{Re} [\mathbf{M}^{(2)} [\mathbf{M}^{(1)}]^3] + 10 \text{Re} [\mathbf{M}^{(3)} [\mathbf{M}^{(1)}]^2] \\ - & 5 \text{Re} [\mathbf{M}^{(4)} \mathbf{M}^{(1)}] + 4 [\mathbf{M}^{(1)}]^5. \end{aligned} \quad (15)$$

Interestingly, with these expressions not only the bandnarrowing is zero in the UEG. Importantly, also the spectral weights $a_{k,j}$ in the n -pole approximation

$$S_k(E) = \hbar \sum_{j=1}^n a_{k,j} \delta(E - E_{k,j}), \quad (16)$$

of the spectral function of the UEG are k -independent when the expressions above are used to obtain the spectral moments $M^{(I)}$ from k -independent moment corrections $M^{(I+)}$. In this case the n bands $E_{k,j}$ corresponding to the n poles are simply parabolas

$$E_{k,j} = \frac{\hbar^2 k^2}{2m} + E_{0,j}, \quad (17)$$

where the Gamma-point energies $E_{0,j}$ of the bands are determined by the moment corrections $M^{(I+)}$.

In the next sections we discuss the three-pole and four-pole approximations in detail and show that one

may even take the limit of an infinite number of poles. Thereby, we show that as the number of poles increases one can reproduce more and more properties of the UEG. In particular, the momentum distribution function, the second moment, and the charge response are very well reproduced when the number of poles is sufficient (Sec. II D). In Sec. II B, Sec. II C, and Sec. II D we will always use Eq. (12) and its generalizations to higher I , e.g. Eq. (14) and Eq. (15), i.e., we will always neglect the bandnarrowing. The observation that we may reproduce the momentum distribution function, the second moment, and the charge response therefore shows that the zero-bandnarrowing approximation suggested in this section works very well for the UEG.

In future refinements of this approach one might include the effect of the bandnarrowing in the UEG. In general, the weights $a_{k,j}$ will then become k -dependent. Moreover, the bands will then not simply be mutually shifted parabolas as in Eq. (17). This will turn the mathematically very simple recipes to construct the moment potentials for MFbSDFT as presented in Sec. II B, Sec. II C, and Sec. II D into very complex high-dimensional multivariate optimization problems, because the necessary integrations can only be performed analytically when the weights $a_{k,j}$ are k -independent and when the band dispersions are available in a simple analytical form, such as Eq. (17). However, this is only the case when the zero-bandnarrowing approximation is used.

The moment potentials $\mathcal{V}^{(I+)}$ tend to become steeper and steeper in r_s with increasing I : An important contribution to the moment potentials is [13]

$$\mathcal{V}^{(I+)}(\mathbf{r}) = \frac{c^{(I+)}}{[r_s(\mathbf{r})]^I} + \dots \quad (18)$$

When one evaluates the integral Eq. (2) within the FLAPW method one expresses $\mathcal{V}^{(I+)}(\mathbf{r})$ on a radial grid inside the MT-spheres. In the interstitial region one employs a representation of $\mathcal{V}^{(I+)}(\mathbf{r})$ in reciprocal space, which is obtained from a fast Fourier transform. A priori one may therefore expect that the convergence of the integral Eq. (2) may be hampered by the steep increase from $[r_s]^{-I}$. However, there is a simple solution to avoid this potential difficulty: We compute the moment potentials $\mathcal{V}^{(I+)}(r_s)$ from the UEG as explained in the following sections. Instead of using them directly in the integral Eq. (2) we compute the I -th root:

$$\bar{\mathcal{V}}^{(I+)}(r_s) = \left[\mathcal{V}^{(I+)}(r_s) \right]^{\frac{1}{I}}. \quad (19)$$

Using the I -th root moment potentials we first compute the matrix elements

$$\bar{M}_{nm}^{(I+)} = \int d^3r \bar{\mathcal{V}}^{(I+)}(\mathbf{r}) [\phi_n(\mathbf{r})]^* \phi_m(\mathbf{r}), \quad (20)$$

and from them we obtain the spectral moment correc-

tions:

$$\mathbf{M}^{(I+)} = \left[\bar{\mathbf{M}}^{(I+)} \right]^I. \quad (21)$$

B. The three-pole approximation

In the three-pole approximation of the UEG the spectral function $S_k(E)$ is given by

$$S_k(E) = \hbar \sum_{j=1}^3 a_{k,j} \delta(E - E_{k,j}), \quad (22)$$

where $a_{k,j}$ and $E_{k,j}$ are the spectral weights and the spectral poles, respectively. This model predicts the momentum distribution to be

$$n_k = \sum_{j=1}^3 f(E_{k,j}) a_{k,j}. \quad (23)$$

We assume that $E_{k,1} < E_F$, $E_{k,3} > E_F$, and $E_{k_F,2} = E_F$, i.e., only $E_{k,2}$ crosses the Fermi level E_F at the Fermi wave number k_F . Consequently, setting $a_{k_F,1} = n_{k_F+}$, $a_{k_F,2} = n_{k_F-} - n_{k_F+}$ and $a_{k_F,3} = 1 - n_{k_F-}$ in Eq. (23) ensures that we reproduce n_{k_F+} , n_{k_F-} , and hence also the step $Z = n_{k_F-} - n_{k_F+}$ of n_k at k_F . Suitable models for n_{k_F-} and n_{k_F+} are given in Ref. [4]. They can be used to determine the spectral weights $a_{k_F,j}$ at the Fermi wave number.

Due to the assumption $E_{k_F,2} = E_F$ we can determine the energy of the second pole at the Fermi wave number by the Fermi energy. When we model the UEG within KS-DFT the bandenergy is given by

$$E_k^{\text{KS}} = \frac{\hbar^2 k^2}{2m} + \frac{d}{dn_e} [n_e E^{\text{xc}}(n_e)], \quad (24)$$

where $E^{\text{xc}}(n_e)$ is the exchange-correlation energy per particle of the UEG with charge density n_e . Consequently, KS-DFT predicts the Fermi energy of the UEG to be $E_F = E_{k_F}^{\text{KS}}$, where

$$k_F = (\bar{\alpha} r_s a_B)^{-1} \quad (25)$$

is the Fermi wave number, and $\bar{\alpha} = [4/(9\pi)]^{1/3}$. E_F as predicted by KS-DFT is consistent with the theorem of Seitz, which relates the Fermi energy to the ground state energy per particle E_g [15]:

$$E_F = \frac{d}{dn_e} [n_e E_g(n_e)]. \quad (26)$$

Therefore, we may expect that KS-DFT predicts the Fermi energy of the UEG sufficiently accurately. This provides us with a relation for the energy of the second pole $E_{k_F,2}$:

$$E_{k_F,2} = \frac{\hbar^2}{2ma_B^2} \frac{1}{[\bar{\alpha} r_s]^2} + V^{\text{xc}}, \quad (27)$$

where

$$V^{\text{xc}} = \frac{d}{dn_e} [n_e E^{\text{xc}}(n_e)] \quad (28)$$

is the exchange-correlation potential.

The Green's function can be obtained easily from the spectral function:

$$G_k(E) = \hbar \sum_{j=1}^3 \frac{a_j}{E - E_{k,j} + i0+}, \quad (29)$$

where we set $a_{k,j} = a_j$, which is valid within the zero-bandnarrowing approximation of the UEG. Defining the noninteracting Green's function by

$$G_{0,k}(E) = \frac{\hbar}{E - E_k^{\text{KS}} + i0+}, \quad (30)$$

we may compute the selfenergy from

$$\Sigma_k(E) = \hbar \left[G_{0,k}^{-1} - G_k^{-1} \right] = E - E_k^{\text{KS}} - \frac{1}{\sum_{j=1,3} \frac{a_j}{E - E_{k,j}}}. \quad (31)$$

We find

$$\left. \frac{\partial \Sigma_{k_F}}{\partial E} \right|_{E=E_F} = 1 - \frac{1}{a_2}. \quad (32)$$

Consequently, the renormalization coefficient at $E = E_F$ is [15]

$$Z_F = \frac{1}{1 - \left. \frac{\partial \Sigma_{k_F}}{\partial E} \right|_{E=E_F}} = a_2 = n_{k_F-} - n_{k_F+}. \quad (33)$$

The Green function of the three-pole approximation yields therefore a renormalization coefficient that is consistent with the jump of the momentum distribution function. This corroborates the overall consistency of our three-pole spectral function.

In order to determine the remaining two poles $E_{k_F,1}$ and $E_{k_F,3}$ we may employ the models for the spectral moments $M_k^{(1)}$ and $M_k^{(2)}$ that have been developed in Ref. [5]. The first moment is

$$M_{k_F}^{(1)} = \frac{\hbar^2 k_F^2}{2m} - \frac{\hbar^2}{ma_B^2} \left[\frac{3}{2\pi} \right]^{\frac{2}{3}} \frac{1}{r_s} \quad (34)$$

and the expressions for $M_{k_F}^{(2)}$ are given in Appendix A. This provides us with the two equations

$$M_{k_F}^{(1)} = a_{k_F,1} E_{k_F,1} + a_{k_F,2} E_{k_F,2} + a_{k_F,3} E_{k_F,3} \quad (35)$$

and

$$M_{k_F}^{(2)} = a_{k_F,1} E_{k_F,1}^2 + a_{k_F,2} E_{k_F,2}^2 + a_{k_F,3} E_{k_F,3}^2 \quad (36)$$

for the two yet unknown poles $E_{k_F,1}$ and $E_{k_F,3}$. In general these equations have two solutions. However, due to

the assumption $E_{k,1} < E_{k,2} < E_{k,3}$ of our model we need to consider only the solution

$$E_{k_F,1} = \frac{-B - \sqrt{B^2 - 4AC}}{2A}, \quad (37)$$

where

$$A = a_{k_F,1} a_{k_F,3} + a_{k_F,1}^2, \quad (38)$$

$$B = -2a_{k_F,1} \left[M_{k_F}^{(1)} - E_{k_F}^{\text{KS}} a_{k_F,2} \right], \quad (39)$$

and

$$C = \left[M_{k_F}^{(1)} - E_{k_F}^{\text{KS}} a_{k_F,2} \right]^2 - M_{k_F}^{(2)} a_{k_F,3} + \left[E_{k_F}^{\text{KS}} \right]^2 a_{k_F,3} a_{k_F,2}. \quad (40)$$

Finally, the energy of the third pole may be computed from

$$E_{k_F,3} = \frac{M_{k_F}^{(1)} - a_{k_F,1} E_{k_F,1} - a_{k_F,2} E_{k_F,2}}{a_{k_F,3}} \quad (41)$$

and the spectral moments $M_{k_F}^{(I)}$ with $I = 3, 4, 5$ may be obtained from

$$M_{k_F}^{(I)} = a_{k_F,1} E_{k_F,1}^I + a_{k_F,2} E_{k_F,2}^I + a_{k_F,3} E_{k_F,3}^I. \quad (42)$$

From these results one may extract the moment potentials $\mathcal{V}^{(3+)}$, $\mathcal{V}^{(4+)}$, and $\mathcal{V}^{(5+)}$ as explained in the preceding section. Using them, one may perform MFbSDFT calculations using the first 6 spectral moments. In Ref. [13] we have already explained in detail how MFbSDFT calculations are performed based on the first 4 spectral moment matrices. The only major change when using the first 6 spectral moments is the construction of the spectral function, which we describe in detail in the Appendix B. While this approach improves the spectra in some cases, it also has a severe shortcoming: The momentum distribution function should be normalized [19], i.e.,

$$\int dk k^2 [n_k - \theta(k_F - k)] = 0 \quad (43)$$

should be satisfied, which is not the case, because Eq. (23) is so constructed that n_k is reproduced at the Fermi surface, while no use is made of this normalization constraint.

In the following we will refer to the bands $E_{k,j} < E_k^{\text{KS}}$ as satellite bands. In the three-pole approximation discussed in this section $E_{k,1}$ is a satellite band, while $E_{k,2}$ could be called the KS-band. The motivation for the name satellite band comes from the observation of a low-energy valence-band satellite peak in the spectrum of Ni, which can be reproduced with the method of spectral moments [20, 21]. While a quantitative relation between

the satellite bands in the n -pole approximation of the UEG and the satellite peaks in the photoemission spectra of several real materials has not yet been established, it seems at least plausible that the satellite bands in the n -pole approximation of the UEG may be considered as precursors of the satellite peaks in the spectra of real materials. The problem of the three-pole approximation proposed above is that it may give too much relative weight to the satellite bands.

We define an averaged momentum distribution by

$$N_< = \frac{3}{k_F^3} \int_0^{k_F} k^2 n_k dk, \quad (44)$$

which considers only $k < k_F$ in the average. A similar averaged momentum distribution can be defined for $k > k_F$:

$$N_> = \frac{3}{k_F^3} \int_{k_F}^{\infty} k^2 n_k dk. \quad (45)$$

Due to the normalization of n_k we have

$$N_< + N_> = 1. \quad (46)$$

While we can satisfy the constraint of Eq. (44) by using the modified weights $a_1 = N_< - Z$, and $a_2 = Z$, and the constraint of Eq. (45) by choosing $E_{0,1}$ appropriately, this choice still attributes too much relative weight to the satellite band, unless the band $E_{k,3}$ cuts the Fermi level. However, if we so specify a k at which $E_{k,3}$ cuts the Fermi level that the satellite band has the appropriate weight, we have determined all three energies $E_{k,j}$ without making use of the first moment $M_{k_F}^{(1)}$. Since the MFbSDFT approach suggested in Ref. [13] assumes that the correct first moment is used in the construction of the moment potentials, not using the right $M_{k_F}^{(1)}$ is not expected to work. In the next section we show that the problem of normalization of n_k can be solved within the 4-pole approximation.

C. The four-pole approximation

In order to determine the energies of the 4 poles we start by setting

$$E_2 = E_{\text{KS}} \quad (47)$$

and

$$a_2 = Z = n_{k_F-} - n_{k_F+} \quad (48)$$

like in the three-pole model. Here, to simplify the notation, we define $E_{\text{KS}} = E_{k_F}^{\text{KS}} = E_F$ and $E_i = E_{k_F,i}$. In order to find E_1 we assume that the corresponding band cuts the Fermi energy at k_{F1} and has the weight

$$a_1 = n_{k_F+}. \quad (49)$$

Therefore, we solve

$$3a_1 \int_{k_F}^{k_{F1}} k^2 dk = a_1(k_{F1}^3 - k_F^3) = k_F^3 N_> \quad (50)$$

for k_{F1} and use it to compute E_1 according to

$$E_1 = E_{\text{KS}} + \frac{\hbar^2 [k_F^2 - k_{F1}^2]}{2m}. \quad (51)$$

The final solution is

$$E_1 = E_{\text{KS}} + \frac{\hbar^2 k_F^2 \left[1 - \left(1 + \frac{1-N_<}{a_1} \right)^{\frac{2}{3}} \right]}{2m}. \quad (52)$$

Using E_1 ensures that the four-pole model $n_k^{(4p)}$ of n_k satisfies Eq. (45).

Next, we determine E_3 assuming that the corresponding band cuts the Fermi energy at k_{F3} and has the weight

$$a_3 = n_0 - n_{k_F-}. \quad (53)$$

Consequently, we require that

$$3(a_1 + a_2) \int_0^{k_F} k^2 dk + 3a_3 \int_0^{k_{F3}} k^2 dk = k_F^3 N_< \quad (54)$$

be satisfied. We use this equation to determine k_{F3} , which is given by

$$k_{F3} = k_F \left[\frac{N_< - a_1 - a_2}{a_3} \right]^{\frac{1}{3}}. \quad (55)$$

Thus, we find

$$E_3 = E_{\text{KS}} + \frac{\hbar^2 k_F^2 \left[1 - \left(\frac{N_< - a_1 - a_2}{a_3} \right)^{\frac{2}{3}} \right]}{2m}. \quad (56)$$

Employing E_3 ensures that the four-pole model $n_k^{(4p)}$ of n_k satisfies Eq. (44).

Finally, we compute E_4 from

$$E_4 = \frac{M_{k_F}^{(1)} - a_1 E_1 - a_2 E_2 - a_3 E_3}{a_4} \quad (57)$$

using

$$a_4 = 1 - a_1 - a_2 - a_3 = 1 - n_0. \quad (58)$$

In the calculations we use the parameterizations of n_0 and n_{k_F+} given in Ref. [4]. Due to the differences in the quasiparticle renormalization Z as obtained from Ref. [4] and Ref. [3] (see the discussion at the beginning of Sec. III and Fig. 5) we take Z from Ref. [3] and use it to compute $n_{k_F-} = n_{k_F+} + Z$. In Fig. 1 we plot the momentum distribution function obtained within the four-pole approximation and compare it to the models of Ref. [4] and Ref. [19, 22]. In the four-pole model n_k can change only

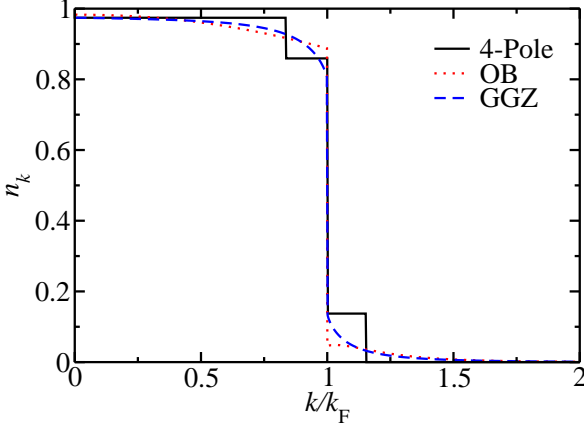


FIG. 1. Comparison of the momentum distribution function obtained within the four-pole model (4-Pole) to the one given in Ref. [19, 22] (OB) and to the one given in Ref. [4] (GGZ). The dimensionless density-parameter is set to $r_s = 3$.

at discrete points k , which is why $n_k^{(4p)}$ exhibits three jumps. Only the major jump at k_F is also present in the models of Ref. [4] and Ref. [19, 22], while n_k changes smoothly otherwise in the latter models. Since one may expect that the correct description of the Fermi surface is particularly important, the two additional jumps in $n_k^{(4p)}$ are not expected to introduce major errors. However, these additional jumps in $n_k^{(4p)}$ are required to ensure the proper normalization of $n_k^{(4p)}$. Clearly, $n_k^{(4p)}$ is a significant improvement over standard KS-DFT, which uses $n_k = \theta(k_F - k)$.

In order to test additional properties of our 4-pole model we start with observing that we have not used the model of $\mathcal{V}^{(2+)}$ discussed in Appendix A in its construction. Consequently, we may compute $\mathcal{V}^{(2+)}$ from our 4-pole model and compare it with the result obtained from the expressions in Appendix A. In Fig. 2 we compare $\mathcal{V}^{(2+)}$ as obtained from the 4-pole model to $\mathcal{V}^{(2+)}$ as given by the expressions in Appendix A. The agreement is surprisingly good in view of the independence of these two models. Note that the expressions in Appendix A are not exact but use the single Slater determinant approximation for one of the higher-order correlation functions. Moreover, different parameterizations of the structure factor are available in the literature and the model of Appendix A yields different results for different parameterizations. In Sec. II D we introduce an $n + 1$ -pole model. We show its results for $\mathcal{V}^{(2+)}$ in Fig. 2 as well. At $r_s = 1$ it agrees with the result from the expressions in Appendix A quite well, while at $r_s = 2$, $r_s = 3$, and $r_s = 4$ it is instead closer to the 4-pole model.

Another property of the UEG that can be used to test our 4-pole model is the charge response $P(\mathbf{q}, \hbar\omega)$, which

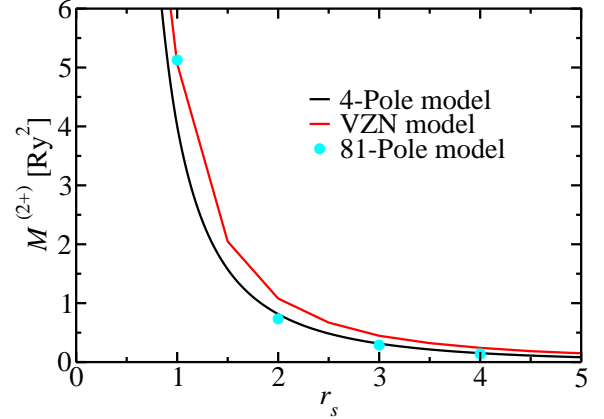


FIG. 2. Comparison between $M_{k_F}^{(2+)} = \mathcal{V}^{(2+)}$ as obtained from the 4-pole model, the $(n + 1)$ -pole model of Sec. II D with 81-poles, and from the model of Ref. [5] discussed in Appendix A (VZN). The vertical axis employs the unit of Ry^2 , where $\text{Ry} = \frac{\hbar^2}{2ma_B^2} = 13.6 \text{ eV}$.

is related to the dielectric function $\epsilon(\mathbf{q}, \hbar\omega)$ by [15]

$$\epsilon(\mathbf{q}, \hbar\omega) = 1 - v_q P(\mathbf{q}, \hbar\omega). \quad (59)$$

Within RPA $\epsilon(\mathbf{q}, \hbar\omega)$ is given by the Lindhard function and the corresponding charge response is

$$\bar{P}(\mathbf{q}, E) = \frac{1}{V} \sum_{\mathbf{k}\sigma} \frac{f(E_{\mathbf{k}\sigma}) - f(E_{\mathbf{k}+\mathbf{q}\sigma})}{E_{\mathbf{k}\sigma} - E_{\mathbf{k}+\mathbf{q}\sigma} + E + i0^+}. \quad (60)$$

When we model the UEG within KS-DFT we obtain

$$\bar{P}_0 = \bar{P}(0, 0) = -D(E_F), \quad (61)$$

where

$$D(E_F) = \frac{4ma_B^2}{(2\pi\hbar)^2 \bar{\alpha} r_s} \quad (62)$$

is the density of states (DOS) at the Fermi energy. However, in KS-DFT the induced charge δn_e changes the exchange-correlation potential, which in turn affects the induced charge [23]. Therefore, the induced charge is related to the single-particle charge response \bar{P}_0 by

$$\delta n_e = \bar{P}_0 \left[\delta\phi + \frac{\partial V^{xc}}{\partial n_e} \delta n_e \right], \quad (63)$$

i.e., the external perturbing field $\delta\phi$ needs to be combined with $(\partial V^{xc}/\partial n_e)\delta n_e$ into the effective perturbation field

$$\delta\phi^{\text{eff}} = \delta\phi + \frac{\partial V^{xc}}{\partial n_e} \delta n_e. \quad (64)$$

Consequently, the full $P_0 = P(0, 0)$ is given by

$$P_0 = \frac{\delta n_e}{\delta\phi} = \frac{\bar{P}_0}{1 - \bar{P}_0 \frac{\partial V^{xc}}{\partial n_e}}. \quad (65)$$

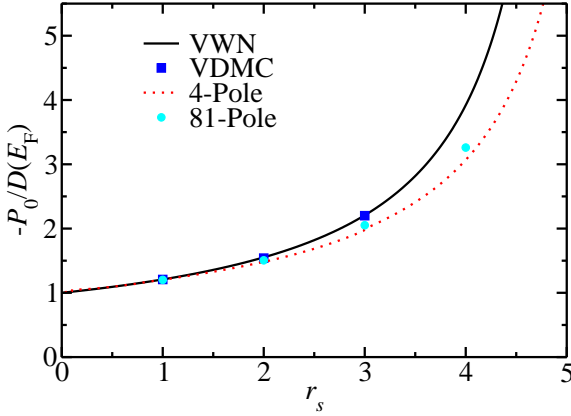


FIG. 3. Ratio of the charge response P_0 and the density of states of the corresponding KS-system at the Fermi energy $D(E_F)$ (Eq. (62)). Four methods are compared. VWN: Eq. (65) using the parameterization of V^{xc} given in Ref. [1]. VDMC: Results from variational diagrammatic Monte Carlo as given in Ref. [24]. 4-Pole: Results for the 4-pole model as computed from Eq. (67). 81-Pole: Results for the $(n+1)$ -pole model as computed from Eq. (81).

In Fig. 3 we show the charge response P_0 as a function of the dimensionless density-parameter r_s as computed from Eq. (65) using the parameterization of V^{xc} given in Ref. [1]. Slightly above $r_s = 5.2$ there is a well-known charge instability, which is why $-P_0/D(E_F)$ starts to increase rapidly for $r_s > 4$. Recent calculations of P_0 by variational diagrammatic Monte Carlo [24] are in excellent agreement (squares in the Figure).

In order to compute P_0 in the 4-pole approximation of the UEG we need to consider all bands that cross the Fermi energy. All bands feel a different effective potential V_i^{xc} . Therefore, we need to modify Eq. (63) as follows:

$$\delta n_e = \sum_{i=1}^{N_{\max}} \bar{P}_{0,i} \left[\delta\phi + \frac{\partial E_{0,j}}{\partial n_e} \delta n_e \right], \quad (66)$$

where N_{\max} is the index of the highest band cutting the Fermi energy ($N_{\max} = 3$ in the derivations above), $\bar{P}_{0,1} = D(E_F)a_1k_{F1}/k_F$, $\bar{P}_{0,2} = D(E_F)a_2$, $\bar{P}_{0,3} = D(E_F)a_3k_{F3}/k_F$, and $E_{0,j}$ is the Gamma-point energy defined in Eq. (17). Consequently, we obtain in the 4-pole approximation

$$P_0^{(4p)} = \frac{\delta n_e}{\delta\phi} = \frac{\sum_{i=1}^{N_{\max}} \bar{P}_{0,i}}{1 - \sum_{i=1}^{N_{\max}} \bar{P}_{0,i} \frac{\partial E_{0,j}}{\partial n_e}}. \quad (67)$$

Fig. 3 shows that the charge response $P_0^{(4p)}$ obtained within our 4-pole model of the UEG is in reasonable agreement with the variational diagrammatic Monte Carlo results.

In Sec. II D we will describe how to increase the number of poles further. However, the results obtained with 81 poles improve the charge response only slightly (circles in Fig. 3). The remaining discrepancies between the n -pole approximation and the VDMC results might result from the zero-bandnarrowing approximation used in this section. Another possible explanation is that the n -pole approximation differs at least partly from the VDMC results because the exact n_k is not known and calculations as well as models of n_k differ in the literature (see e.g. Fig. 5).

Overall, our four-pole model reproduces the momentum distribution n_k (Fig. 1), the charge response function P_0 (Fig. 3), and the second moment (Fig. 2) quite well. In contrast, we can reproduce only P_0 within the KS-DFT model of the UEG.

D. The n -pole model and the limit $n \rightarrow \infty$

The agreement between the properties of the UEG and those predicted by the 4-pole model can be improved further by considering the following $(n+1)$ -pole model (n is an even number). We assume that band $n/2$ is the KS-band, i.e.,

$$E_{\frac{n}{2}} = E_{\text{KS}} \quad (68)$$

and

$$a_{\frac{n}{2}} = Z. \quad (69)$$

The bands $n/2 + 1, \dots, n$ are higher in energy than the KS-band, but they are all assumed to cut the Fermi energy. The bands $1, \dots, n/2 - 1$ are lower in energy than the KS-band and therefore they cut the Fermi level as well.

We devide the range from $k = 0$ to $k = k_F$ into $n/2$ pieces, where the i -th piece is defined by the lower boundary

$$k_{\min,i} = k_F \frac{1 - \delta}{\frac{n}{2}} (n - i) \quad (70)$$

and the upper boundary

$$k_{\max,i} = k_F \frac{1 - \delta}{\frac{n}{2}} (n + 1 - i), \quad (71)$$

where $i = \frac{n}{2} + 1, \dots, n$, and the positive infinitesimal δ ensures that $k_{\max,\frac{n}{2}+1} < k_F$.

Typically, $n_{(2k_F)} \ll n_{k_F}$. Consequently, we consider the interval from $k = k_F$ up to $k = 2k_F$ and divide it into $n/2 - 1$ pieces, where the i -th piece is defined by the lower boundary

$$k_{\min,i} = k_F \left[1 + \delta + \frac{\frac{n}{2} - 1 - i}{\frac{n}{2} - 1} \right] \quad (72)$$

and the upper boundary

$$k_{\max,i} = k_F \left[1 + \delta + \frac{\frac{n}{2} - i}{\frac{n}{2} - 1} \right]. \quad (73)$$

Here, $i = 1, \dots, \frac{n}{2} - 1$, and the positive infinitesimal δ ensures that $k_{\min,\frac{n}{2}-1} > k_F$.

We define the corresponding weights as

$$a_i = n_{k_{\min,i}} - n_{k_{\max,i}} \quad (74)$$

for $i = 2, \dots, \frac{n}{2} - 1$ and for $i = \frac{n}{2} + 1, \dots, n$. These weights are always positive if the derivative

$$\frac{dn_k}{dk} < 0 \quad (75)$$

is always negative. This is the case for the parameterization of n_k given in Ref. [4]. The weight of the first band we set to

$$a_1 = n_0 - \sum_{i=2}^n a_n. \quad (76)$$

The corresponding energies at k_F are given by

$$E_i = E_{\text{KS}} + \frac{\hbar^2}{2m} \left[k_F^2 - \frac{(k_{\min,i} + k_{\max,i})^2}{4} \right] \quad (77)$$

for $i = 1, \dots, \frac{n}{2} - 1$ and for $i = \frac{n}{2} + 1, \dots, n$. Finally, we assume that the band $n+1$ is highest in energy and does not cut the Fermi energy. We set its weight to

$$a_{n+1} = 1 - n_0 \quad (78)$$

and determine its energy from the first moment:

$$E_{n+1} = \frac{1}{a_{n+1}} \left[M_{k_F}^{(1)} - \sum_{i=1}^n a_n E_n \right]. \quad (79)$$

The moments $M_{k_F}^{(I)}$ for $I > 1$ can be computed from

$$M_{k_F}^{(I)} = \sum_{j=1}^{n+1} a_j E_j^I, \quad (80)$$

while the charge response may be obtained from

$$P_0^{([n+1]\text{p})} = \frac{\delta n_e}{\delta \phi} = \frac{\mathcal{G}}{1 - \frac{\partial V^{\text{xc}}}{\partial n_e} \mathcal{G}}, \quad (81)$$

where

$$\mathcal{G} = D(E_F) \sum_{i=1}^n a_i \frac{k_{\min,i} + k_{\max,i}}{2k_F}. \quad (82)$$

In Fig. 4 we illustrate the basic idea of the $(n+1)$ -pole model by comparing the momentum distribution function n_k that it produces to the one of Ref. [4]: The bands

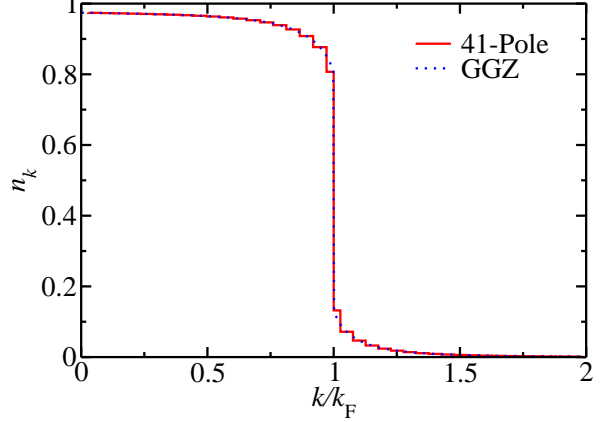


FIG. 4. Comparison of the momentum distribution function obtained within the 41-pole model to the one given in Ref. [4] (GGZ). The dimensionless density-parameter is set to $r_s = 3$.

in the $(n+1)$ -pole model of the zero-bandnarrowing approximation of the UEG are given by the set of parabolas, Eq. (17). n of these bands cut the Fermi level. When one of these bands cuts the Fermi level at a given k , i.e., when $E_{k,i} = E_F$, the momentum distribution is reduced by the weight a_i of this band. As Fig. 4 shows, with $n = 40$ the model of Ref. [4] can be reproduced reasonably well. One may of course increase the number of poles further, until these two curves become indistinguishable. However, the effect of increasing the number of poles on $M_{k_F}^{(2+)}$ and the charge response P_0 is small, as Fig. 2 and Fig. 3 show. Thus, reproducing Z , $N_<$, and $N_>$ by the 4-pole approximation is already a major improvement over KS-DFT, while increasing the number of poles further mainly improves n_k below and above the Fermi surface, as the comparison between Fig. 1 and Fig. 4 shows.

Interestingly, we may even take the limit $n \rightarrow \infty$ and consider a continuum model. In the continuum model the energy of the highest band is

$$E_\infty = \frac{1}{n_\infty} \left[\int_0^{k_{F-}} \left(E_{\text{KS}} + \frac{\hbar^2}{2m} (k_F^2 - k^2) \right) \frac{dn_k}{dk} dk + \int_{k_{F+}}^\infty \left(E_{\text{KS}} + \frac{\hbar^2}{2m} (k_F^2 - k^2) \right) \frac{dn_k}{dk} dk - E_{\text{KS}} Z + M_{k_F}^{(1)} \right], \quad (83)$$

which may be rewritten as

$$E_\infty = \frac{1}{n_\infty} \left[-E_{\text{KS}} Z + M_{k_F}^{(1)} - n_0 \left(E_{\text{KS}} + \frac{\hbar^2 k_F^2}{2m} \right) - \int_0^{k_{F-}} \frac{\hbar^2}{2m} k^2 \frac{dn_k}{dk} dk - \int_{k_{F+}}^\infty \frac{\hbar^2}{2m} k^2 \frac{dn_k}{dk} dk \right], \quad (84)$$

where

$$n_\infty = 1 - n_0. \quad (85)$$

The I -th moment is given by

$$M^{(I)} = n_\infty E_\infty^I + Z E_{\text{KS}}^I - \int_0^{k_F} \frac{dn_k}{dk} \mathcal{E}_k^I dk - \int_{k_F}^\infty \frac{dn_k}{dk} \mathcal{E}_k^I dk, \quad (86)$$

where

$$\mathcal{E}_k = E_{\text{KS}} + \frac{\hbar^2}{2m} [k_F^2 - k^2]. \quad (87)$$

E. An optimized two-pole model

In weakly and moderately correlated systems the low-energy satellite band is often of little interest, while a good description of bandgaps and bandwidths is desirable. In this case, the most important benefits of the four-pole approximation may be reproduced effectively by an optimized two-pole model. In this model we leave away the low-energy satellite band completely. We assume that at the Fermi surface we have $E_1 = E_{\text{KS}}$ (Seitz-theorem). For a_1 we may either choose n_{k_F} or Z . It might be that one of these two possible options is better, which we have not investigated systematically yet. The argument to use $a_1 = Z$ is that the weight of the quasiparticles on the Fermi surface at k_F is Z in the 4-pole approximation. However, one may also argue that $a_1 = n_{k_F}$ might be more correct, because the weight of the low-energy satellite band should be included into a_1 , if it is not described explicitly. In this work we choose $a_1 = Z$.

We assume that the band E_1 cuts the Fermi level at $k_T > k_F$, because this is the only way to achieve normalization of n_k when the low-energy satellite band is not described explicitly. In general both bands, E_1 and E_2 , may cut the Fermi energy. When both bands cut the Fermi level

$$a_2 [k_F^3 - a_1 k_T^3]^2 = [k_F^2 + V^c - a_1 k_T^2]^3 \quad (88)$$

is a nonlinear equation for k_T , which can be solved numerically. Here, $a_2 = 1 - a_1$, and

$$V^c = \frac{d}{dn_e} [n_e E^c(n_e)] \quad (89)$$

is the correlation potential, where $E^c(n_e)$ is the correlation energy per particle in the UEG with electron density n_e .

In practice, one may first solve Eq. (88) at all relevant parameters r_s . Next, at a given r_s one checks if

$$E_2 - \frac{\hbar^2 k_T^2}{2m} > E_{\text{KS}} \quad (90)$$

is satisfied. If it is, the band E_2 does not cut the Fermi energy. In these cases, one needs to replace k_T by

$$k_T = \frac{k_F}{a_1^{1/3}}. \quad (91)$$

The energy of the second band is computed from

$$E_2 = \frac{\bar{M}_{k_F}^{(1)} - a_1 E_{\text{KS}}}{a_2}, \quad (92)$$

where

$$\bar{M}_{k_F}^{(1)} = \frac{\hbar^2 k_T^2}{2m} - \frac{\hbar^2}{ma_B^2} \left[\frac{3}{2\pi} \right]^{\frac{2}{3}} \frac{1}{r_s}. \quad (93)$$

Ignoring the low-energy satellite bands according to these equations affects the determination of the Fermi energy: In insulators one will automatically include part of the conduction band electrons into the ground state charge density in order to achieve charge neutrality. In the calculation of the DOS, this problem can be avoided simply by setting $a_j = 1$ in the determination of the Fermi level. By this choice one assumes that the missing charge is provided by the satellite bands and amounts effectively to

$$a_j \rightarrow 1. \quad (94)$$

When computing the charge density in the self-consistency loop we could in principle use a_j as obtained from the state vectors [13]. However, in order to minimize the inconsistency between these two options, we use

$$a_j \rightarrow \frac{1}{2} [1 + a_j] \quad (95)$$

in the selfconsistency loop.

III. RESULTS

Unless stated otherwise, the results shown in this section are obtained with the optimized two-pole model of Sec. II E. An important ingredient of this model is the quasiparticle renormalization factor Z , for which many calculations have been performed [3, 25]. Ref. [3] reports a very small error bar for recent variational diagrammatic Monte Carlo computations of this quantity. In Fig. 5 we compare these recent results to the model of Ref. [4]. At the parameters $r_s = 2$, $r_s = 3$, and $r_s = 4$ the deviations are large, while the agreement is good at $r_s = 1$.

We need a model for $Z(r_s)$ which captures the full range of variation of r_s in our first-principles calculations. The minimal and maximal values of r_s are listed in Table I for all systems studied in this work. Clearly, we need Z also for values below and above the range considered

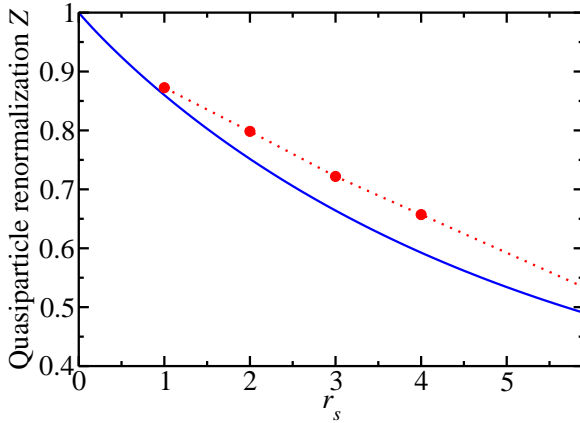


FIG. 5. Quasiparticle renormalization factor Z as obtained from the model of Ref. [4] (solid line) and from the variational diagrammatic Monte Carlo calculations of Ref. [3] (circles). Dotted lines are linear interpolations and extrapolations of the variational diagrammatic Monte Carlo data.

in Ref. [3], which lists values of Z only for $r_s = 1$, $r_s = 2$, $r_s = 3$, and $r_s = 4$. Therefore, we construct a model of $Z(r_s)$ as follows: For $r_s < 1$ we use the model of Ref. [4]. This is justified, because at $r_s = 1$ this model does not deviate much from the variational diagrammatic Monte Carlo results of Ref. [3] (see Fig. 5). The variational diagrammatic Monte Carlo results in the range $1 \leq r_s \leq 4$ almost follow a linear trend. Therefore, we use linear interpolation to determine $Z(r_s)$ for values in the range $1 < r_s < 4$ (dotted lines in Fig. 5). According to Table I we need $Z(r_s)$ up to $r_s = 5.07$. Therefore, we linearly extrapolate the variational diagrammatic Monte Carlo results for $r_s > 4$.

A. Silicon, Diamond, and Silicon Carbide

Silicon crystallizes in the diamond structure with the lattice parameter $a = 5.43$ Å. Employing the PBE [26] functional we obtain a bandgap of 0.6 eV within KS-DFT. This is smaller than the experimental bandgap of 1.17 eV by roughly a factor of 2. In Fig. 6 we compare the DOS obtained from MFbSDFT to the one obtained from KS-DFT. Within MFbSDFT the bandgap is 1.22 eV, which is close to the experimental value.

In the cubic 3C-SiC polymorph of silicon carbide one half of the sites of the diamond lattice are occupied by Si and the other half by C. The lattice constant is $a = 4.36$ Å. Experimentally, the band gap is determined to be 2.36 eV. Employing the PBE functional we obtain a bandgap of 1.4 eV in KS-DFT. The bandgap of 2.8 eV obtained within MFbSDFT is too large compared to the experiment, but significantly closer to the experimental

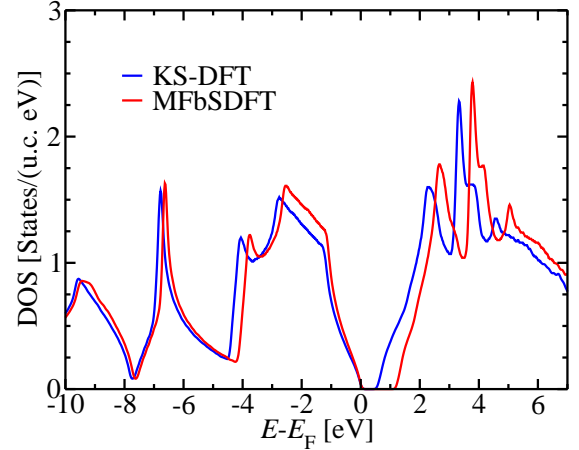


FIG. 6. Density of states (DOS) of Si vs. energy E as obtained in KS-DFT and in MFbSDFT. E_F is the Fermi energy.

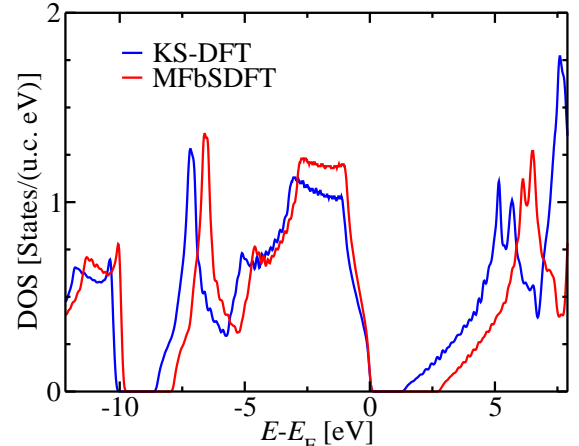


FIG. 7. Density of states (DOS) of SiC vs. energy E as obtained in KS-DFT and in MFbSDFT. E_F is the Fermi energy.

value than the PBE result. In Fig. 7 we compare the DOS obtained from MFbSDFT to the one obtained from KS-DFT.

The lattice parameter of diamond is $a = 3.567$ Å. Employing the PBE functional we obtain a bandgap of 5.7 eV in KS-DFT, which is in good agreement with the experimental bandgap of 5.47 eV. Within MFbSDFT we obtain a bandgap of 5.14 eV, which also agrees acceptably well with experiment, while the agreement is slightly better for the PBE result. In Fig. 8 we compare the DOS obtained from MFbSDFT to the one obtained from KS-DFT.

It is remarkable that KS-DFT almost reproduces the experimental bandgap in diamond, but is significantly off in the isoelectric compounds SiC and Si. To some extent this depends on the functional used. For example KS-

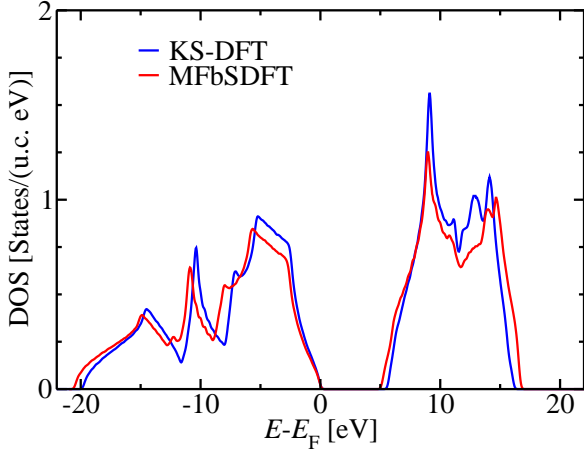


FIG. 8. Density of states (DOS) of diamond vs. energy E as obtained in KS-DFT and in MFbSDFT. E_F is the Fermi energy.

DFT predicts a bandgap of only 4.11 eV when LDA is employed. However, this underestimation of the bandgap by 25% is still relatively small compared to the typical bandgap error in KS-DFT.

Since an important contribution to the moment functional corrections comes from the quasiparticle renormalization factor Z , the question arises of whether this correction might be particularly small in diamond, which might contribute to the good performance of PBE for the bandgap in this wide-gap semiconductor. According to Fig. 5 the Z factor starts to deviate strongly from 1 when r_s becomes larger than 1. Therefore, we show in Table I the minimal and maximal values of r_s . Indeed, diamond is characterized by a relatively small value of $r_{s,\max} = 2.44$. Thus, to some extent Table I suggests that the importance of taking $Z < 1$ into account when r_s increases is reflected in the error $\Delta E_{\text{PBE}}^{\text{gap}}/E_{\text{exp}}^{\text{gap}}$. A more quantitative investigation of this hypothesis might be possible by computing the unit-cell average

$$\frac{1}{V} \int d^3r [1 - Z(r_s)], \quad (96)$$

which we do not consider here and leave for future work.

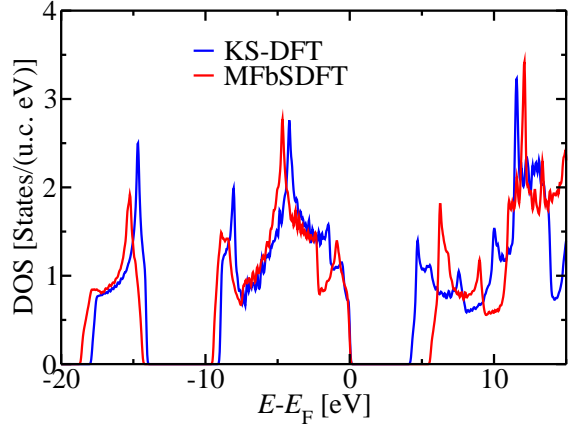


FIG. 9. Density of states (DOS) of BN vs. energy E as obtained in KS-DFT and in MFbSDFT. E_F is the Fermi energy.

TABLE I. Minimal ($r_{s,\min}$) and maximal ($r_{s,\max}$) values of the dimensionless density parameter r_s in the MFbSDFT calculations. Deviation $\Delta E_{\text{PBE}}^{\text{gap}} = E_{\text{PBE}}^{\text{gap}} - E_{\text{exp}}^{\text{gap}}$ of the bandgap obtained with KS-DFT ($E_{\text{PBE}}^{\text{gap}}$) from the experimental bandgap ($E_{\text{exp}}^{\text{gap}}$). Deviation $\Delta E_{\text{SDFT}}^{\text{gap}} = E_{\text{SDFT}}^{\text{gap}} - E_{\text{exp}}^{\text{gap}}$ of the bandgap obtained with MFbSDFT ($E_{\text{SDFT}}^{\text{gap}}$) from the experimental bandgap ($E_{\text{exp}}^{\text{gap}}$). Large relative errors $|\Delta E_{\text{PBE}}^{\text{gap}}/E_{\text{exp}}^{\text{gap}}|$ tend to occur when $r_{s,\max}$ is large.

	$r_{s,\min}$	$r_{s,\max}$	$\Delta E_{\text{PBE}}^{\text{gap}}/E_{\text{exp}}^{\text{gap}}$	$\Delta E_{\text{SDFT}}^{\text{gap}}/E_{\text{exp}}^{\text{gap}}$
C	0.12	2.44	4%	-6%
Si	0.05	4.28	-49%	4%
SiC	0.05	3.29	-41%	19%
BN	0.1	5.07	-29%	-6%
MgO	0.059	2.72	-38%	-11%
CaO	0.03	3.32	-48%	-13%
ZnO	0.019	3.72	-73%	2%

B. Boron nitride

We consider hexagonal BN, which exhibits a layered structure similar to graphite. It is a semiconductor with a wide bandgap of 5.955 eV [27]. The in-plane lattice parameter is $a = 2.504 \text{ \AA}$ and the interlayer distance is $a = 3.33 \text{ \AA}$. KS-DFT with the PBE functional significantly underestimates the bandgap and predicts it to be 4.25 eV. In contrast, the bandgap obtained from MFbSDFT is 5.61 eV, which is in good agreement with experiment. In Fig. 9 we compare the DOS of the MFbSDFT calculation to the one obtained within KS-DFT.

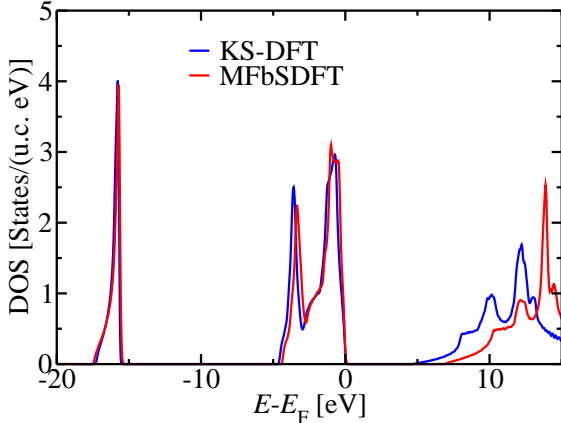


FIG. 10. Density of states (DOS) of MgO vs. energy E as obtained in KS-DFT and in MFbSDFT. E_F is the Fermi energy.

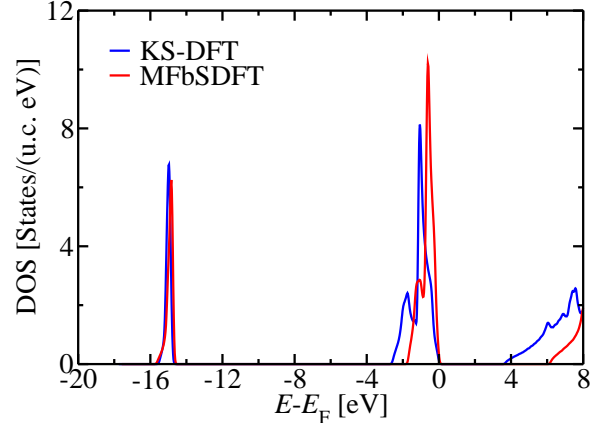


FIG. 11. Density of states (DOS) of CaO vs. energy E as obtained in KS-DFT and in MFbSDFT. E_F is the Fermi energy.

C. MgO and CaO

MgO crystallizes in the rocksalt structure with the lattice parameter $a = 4.212$ Å. Using KS-DFT with the PBE functional we obtain a bandgap of 4.8 eV, which is much smaller than the experimental bandgap of 7.77 eV. In MFbSDFT we obtain a bandgap of 6.95 eV. This is in acceptable agreement with experiment considering that GW calculations deviate from the experimental bandgap as well in this case even when quasiparticle self-consistency is imposed [16]. In Fig. 10 we compare the DOS of the MFbSDFT calculation to the one obtained within KS-DFT.

The isoelectric compound CaO crystallizes in the rock-salt structure with the lattice parameter $a = 4.815$ Å. Using KS-DFT with the PBE functional we obtain a bandgap of 3.67 eV, which is much smaller than the experimental bandgap of 7.1 eV. In MFbSDFT we obtain a bandgap of 6.17 eV, which is a significant improvement. In Fig. 11 we compare the DOS of the MFbSDFT calculation to the one obtained within KS-DFT.

D. ZnO

ZnO crystallizes in the wurtzite crystal structure. The lattice parameters are $a = 3.25$ Å and $c = 5.2$ Å. When we employ the PBE functional we obtain a bandgap of 0.88 eV from KS-DFT, which is much smaller than the experimental bandgap of 3.3 eV. In MFbSDFT we obtain a bandgap of 3.37 eV, which is very close to the experimental value. In Fig. 12 we compare the DOS of the MFbSDFT and of the KS-DFT calculations.

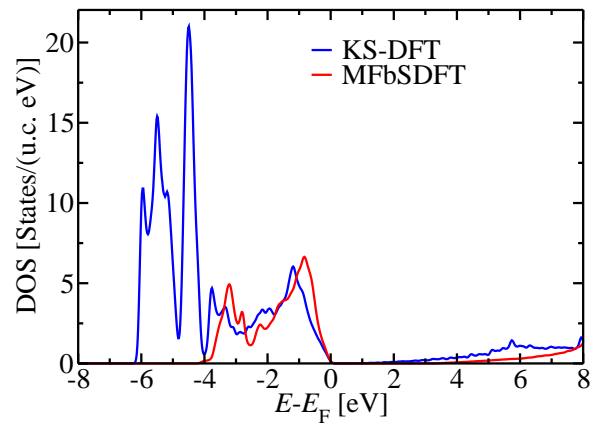


FIG. 12. Density of states (DOS) of ZnO vs. energy E as obtained in KS-DFT and in MFbSDFT. E_F is the Fermi energy.

E. The optimized two-pole model vs. the three-pole approximation

In Ni correlation effects are very important and standard KS-DFT fails to predict the correct exchange splitting, the correct bandwidth, and the valence-band satellite peak [20, 21]. Our optimized two-pole model of Sec. II E excludes the low-energy satellite band by construction. At the same time it is possible to obtain the satellite peak in Ni using the first four spectral moments obtained from a lattice model [20, 21]. The question therefore arises of whether our prescription in Sec. II E to construct the moment potentials for MFbSDFT suppresses the valence band satellite in Ni.

In Fig. 13 we show that the valence band satellite is in-

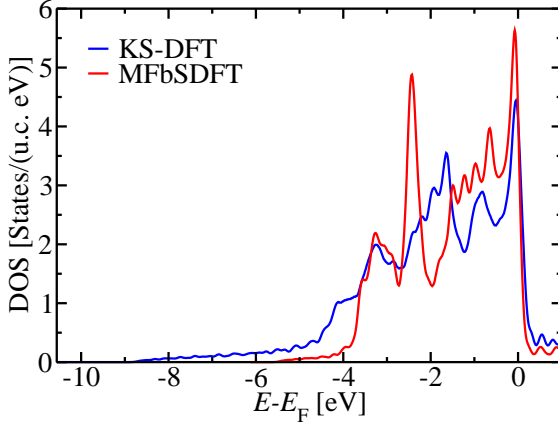


FIG. 13. Density of states (DOS) in the spin-unpolarized phase of Ni. KS-DFT and MFbSDFT (optimized 2-pole model) are compared.

deed absent when the moment potentials are constructed from the model of Sec. II E. However, the comparison to KS-DFT shows that at least the bandwidth is smaller in MFbSDFT and therefore in better agreement with experiment. Since we do not consider the spin-polarized case in this work, Fig. 13 illustrates the DOS of a spin-unpolarized phase of Ni. This interesting result shows that the presence or absence of a valence band satellite peak in the spectrum is not only dependent on the number of poles used, but also on the prescription used to obtain the moment potentials.

In Sec. II B we have discussed that the 3-pole model gives too much weight to the satellite band. This can be seen clearly in Fig. 14. While the experimentally observed satellite peak slightly below -6 eV is now present in the MFbSDFT spectrum, there is overall too much spectral density below -4 eV relative to the main band. A possible solution might be to optimize the 3-pole model using part of the ideas of Sec. II E, which we leave for future work.

IV. SUMMARY

Considering the 3-pole and the 4-pole approximations of the spectral function of the UEG we corroborate the idea that more and more properties of the UEG can be described when the number of poles is increased. Our 4-pole model describes the charge response, the momentum distribution, and the second moment of the UEG acceptably well, while the KS-DFT approximation of the UEG describes from these quantities only the charge response well. Focusing on the most important aspects that the 4-pole approximation improves in comparison to KS-DFT in weakly and moderately correlated systems

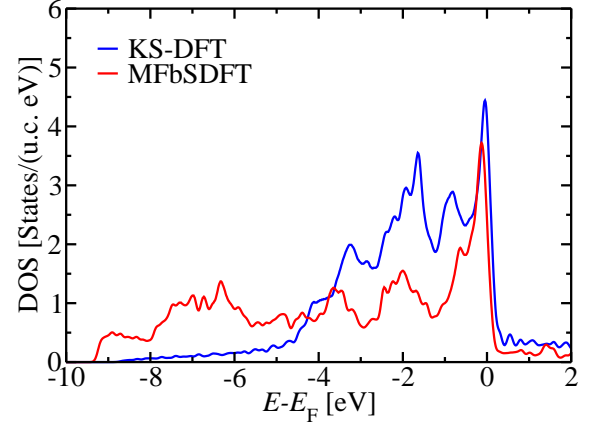


FIG. 14. Density of states (DOS) in the spin-unpolarized phase of Ni. KS-DFT and MFbSDFT (3-pole model) are compared.

we construct an optimized 2-pole approximation which we use to extract *parameter-free universal* moment potentials for MFbSDFT. Using these we show that the bandgaps in the insulators Si, SiC, BN, MgO, CaO, and ZnO are significantly closer to the experimental bandgaps in MFbSDFT than in KS-DFT with the PBE functional. Finally, we show that the 3-pole approximation highly overestimates the satellite bands in strongly correlated materials and therefore it needs to be optimized to mimic the behaviour of the 4-pole approximation. In this work we consider only the spin unpolarized case. The inclusion of magnetism is an important extension left for future work.

Appendix A: Model of the second moment for the UEG

Ref. [5] derives a model for the second spectral moment of the UEG, where $M_k^{(2)}$ is expressed in terms of the exchange self-energy, the pair correlation function, and a remaining higher correlation function, which is assessed by the single-Slater-determinant approximation. From this model we obtain

$$M_k^{(2+)} = \Sigma_{\text{loc}}^{(1)} + \Sigma_{\text{nl},k}^{(1)}, \quad (\text{A1})$$

where

$$\Sigma_{\text{loc}}^{(1)} = \left[\frac{\hbar^2}{2ma_B^2} \right]^2 \frac{32}{3\pi^2} \frac{k_F}{(\bar{a}r_s)^2} \int_0^\infty \frac{dk'}{k'^2} S(k') \quad (\text{A2})$$

is a k -independent contribution [5], and

$$\begin{aligned} \Sigma_{\text{nl},k}^{(1)} = & -\left[\Sigma_k^{(0)}\right]^2 - \left[\frac{\hbar^2}{2ma_B^2}\right]^2 \frac{2}{(\bar{\alpha}r_s)^3 \pi k k_F} \times \\ & \times \int_0^\infty dk' k' \Sigma_{k'}^{(0)} (1 - 2n_{k'}) \ln \left| \frac{k - k'}{k + k'} \right| \end{aligned} \quad (\text{A3})$$

is a k -dependent contribution [5]. Here, $\bar{\alpha} = [4/(9\pi)]^{1/3}$, $k_F = (\bar{\alpha}r_s a_B)^{-1}$,

$$S(k) = 1 + 4\pi n_e \int dr r \frac{\sin(kr)}{k} [g(r) - 1], \quad (\text{A4})$$

is the structure factor, $g(r)$ is the pair correlation function, and

$$\Sigma_k^{(0)} = -\frac{\hbar^2}{2ma_B^2} \frac{2}{\pi k k_F \bar{\alpha} r_s} \int_0^\infty dk' k' n_{k'} \ln \left| \frac{k + k'}{k - k'} \right| \quad (\text{A5})$$

is the exchange self-energy.

In order to extract the moment potential $\mathcal{V}^{(2+)}$ from this model we set $k = k_F$, because we need k -independent moment potentials. Thus, we use

$$\mathcal{V}^{(2+)} = \Sigma_{\text{loc}}^{(1)} + \Sigma_{\text{nl},k_F}^{(1)}. \quad (\text{A6})$$

$\mathcal{V}^{(2+)}$ depends on r_s because Eq. (A2) and Eq. (A3) depend explicitly on r_s . Additionally, it depends on r_s because k_F and $S(k)$ depend on r_s . In the literature several models have been suggested for the pair correlation function $g(r)$ and for the structure factor $S(k)$. We use the model of Ref. [28] in the numerical results shown in Fig. 2.

Appendix B: MFbSDFT with the first 6 spectral moments

In Ref. [14] we describe an efficient algorithm to obtain the spectral function from the first $2P$ spectral moment matrices of size $N \times N$. In the special case of $P = 3$, i.e., when the first 6 spectral moment matrices $\mathbf{M}_k^{(0)}$, $\mathbf{M}_k^{(1)}$, $\mathbf{M}_k^{(2)}$, $\mathbf{M}_k^{(3)}$, $\mathbf{M}_k^{(4)}$, $\mathbf{M}_k^{(5)}$ are used, the $3N$ poles $E_{k,j}$ ($j = 1, \dots, 3N$) of the spectral function are given by the eigenvalues of the $3N \times 3N$ matrix

$$\mathcal{H}_k = \begin{pmatrix} \mathbf{M}_k^{(1)} & \mathbf{B}_{1,k} \\ \mathbf{B}_{1,k}^\dagger & \mathbf{D}_{1,k} \end{pmatrix}, \quad (\text{B1})$$

where $\mathbf{B}_{1,k}$ is a $N \times 2N$ matrix, and $\mathbf{D}_{1,k}$ is a $2N \times 2N$ matrix. $\mathbf{B}_{1,k}$ is given by the first N rows of the $2N \times 2N$ matrix \mathcal{B} , which may be computed by taking the square root of the hermitian positive definite matrix

$$\mathcal{B} \mathcal{B}^\dagger = \begin{pmatrix} \mathbf{M}_k^{(2)} - [\mathbf{M}_k^{(1)}]^2 & \mathbf{M}_k^{(3)} - \mathbf{M}_k^{(1)} \mathbf{M}_k^{(2)} \\ \mathbf{M}_k^{(3)} - \mathbf{M}_k^{(2)} \mathbf{M}_k^{(1)} & \mathbf{M}_k^{(4)} - [\mathbf{M}_k^{(2)}]^2 \end{pmatrix}. \quad (\text{B2})$$

The matrix $\mathbf{D}_{1,k}$ may be computed from

$$\mathbf{D}_{1,k} = \mathcal{B}^{-1} \begin{pmatrix} \mathbf{B}_{2,k} - \mathbf{M}_k^{(1)} \mathbf{B}_{1,k} \\ \mathbf{B}_{3,k} - \mathbf{M}_k^{(2)} \mathbf{B}_{1,k} \end{pmatrix}, \quad (\text{B3})$$

where the $N \times 2N$ matrix $\mathbf{B}_{2,k}$ is given by the last N rows of the matrix \mathcal{B} and the $N \times 2N$ matrix $\mathbf{B}_{3,k}$ may be computed from the $2N \times N$ matrix

$$\mathbf{B}_{3,k}^\dagger = \mathcal{B}^{-1} \begin{pmatrix} \mathbf{M}_k^{(4)} - \mathbf{M}_k^{(1)} \mathbf{M}_k^{(3)} \\ \mathbf{M}_k^{(5)} - \mathbf{M}_k^{(2)} \mathbf{M}_k^{(3)} \end{pmatrix} \quad (\text{B4})$$

by taking the complex conjugate.

The single-particle spectral function is given by

$$\frac{S_{kij}(E)}{\hbar} = \sum_{l=1}^{3N} a_{kl} \mathcal{V}_{kil} \mathcal{V}_{kjl}^* \delta(E - E_{kl}), \quad (\text{B5})$$

where

$$\mathcal{V}_{kij} = \frac{U_{kij}}{\sqrt{a_{kj}}}, \quad (\text{B6})$$

with $i = 1, \dots, N$, $j = 1, \dots, 3N$, is the matrix of state vectors, and

$$a_{kj} = \sum_{i=1}^N U_{kij} [U_{kij}]^* \quad (\text{B7})$$

are the spectral weights. The $3N \times 3N$ matrix \mathbf{U}_k holds the $3N$ eigenvectors of \mathcal{H}_k in its $3N$ columns.

ACKNOWLEDGMENTS

The project is funded by the Deutsche Forschungsgemeinschaft (DFG, German Research Foundation) – TRR 288 – 422213477 (project B06), CRC 1238, Control and Dynamics of Quantum Materials: Spin orbit coupling, correlations, and topology (Project No. C01), SPP 2137 “Skyrmionics”, and Sino-German research project DISTOMAT (DFG project MO 1731/10-1). We also acknowledge financial support from the European Research Council (ERC) under the European Union’s Horizon 2020 research and innovation program (Grant No. 856538, project “3D MAGiC”) and computing resources granted by the Jülich Supercomputing Centre under project No. jiff40.

* Corresp. author: f.freimuth@fz-juelich.de
[1] S. H. Vosko, L. Wilk, and M. Nusair, Accurate spin-dependent electron liquid correlation energies for local spin density calculations: a critical analysis, Canadian Journal of Physics **58**, 1200 (1980).

[2] J. P. Perdew and Y. Wang, Accurate and simple analytic representation of the electron-gas correlation energy, *Phys. Rev. B* **45**, 13244 (1992).

[3] K. Haule and K. Chen, Single-particle excitations in the uniform electron gas by diagrammatic monte carlo, *Scientific Reports* **12**, 2294 (2022).

[4] P. Gori-Giorgi and P. Ziesche, Momentum distribution of the uniform electron gas: Improved parametrization and exact limits of the cumulant expansion, *Phys. Rev. B* **66**, 235116 (2002).

[5] M. Vogt, R. Zimmerman, and R. J. Needs, Spectral moments in the homogeneous electron gas, *Phys. Rev. B* **69**, 045113 (2004).

[6] A. Georges, G. Kotliar, W. Krauth, and M. J. Rozenberg, Dynamical mean-field theory of strongly correlated fermion systems and the limit of infinite dimensions, *Rev. Mod. Phys.* **68**, 13 (1996).

[7] G. Kotliar, S. Y. Savrasov, K. Haule, V. S. Oudovenko, O. Parcollet, and C. A. Marianetti, Electronic structure calculations with dynamical mean-field theory, *Rev. Mod. Phys.* **78**, 865 (2006).

[8] F. Krien, E. G. C. P. van Loon, M. I. Katsnelson, A. I. Lichtenstein, and M. Capone, Two-particle fermi liquid parameters at the mott transition: Vertex divergences, landau parameters, and incoherent response in dynamical mean-field theory, *Phys. Rev. B* **99**, 245128 (2019).

[9] P. Hohenberg and W. Kohn, Inhomogeneous electron gas, *Phys. Rev.* **136**, B864 (1964).

[10] W. Kohn and L. J. Sham, Self-consistent equations including exchange and correlation effects, *Phys. Rev.* **140**, A1133 (1965).

[11] S. Mandal, K. Haule, K. M. Rabe, and D. Vanderbilt, Electronic correlation in nearly free electron metals with beyond-dft methods, *npj Computational Materials* **8**, 181 (2022).

[12] G. D. Mahan and B. E. Sernelius, Electron-electron interactions and the bandwidth of metals, *Phys. Rev. Lett.* **62**, 2718 (1989).

[13] F. Freimuth, S. Blügel, and Y. Mokrousov, Moment functional based spectral density functional theory, *Phys. Rev. B* **106**, 155114 (2022).

[14] F. Freimuth, S. Blügel, and Y. Mokrousov, Moment potentials for spectral density functional theory: Exploiting the momentum distribution of the uniform electron gas (2022), arXiv:2212.12624v1 [cond-mat.mtrl-sci].

[15] G. D. Mahan, *Many-Particle Physics*, Physics of Solids and Liquids (Kluwer Academic/Plenum Publishers, 2000).

[16] M. van Schilfgaarde, T. Kotani, and S. Faleev, Quasiparticle self-consistent *gw* theory, *Phys. Rev. Lett.* **96**, 226402 (2006).

[17] A. Sekiyama, H. Fujiwara, S. Imada, S. Suga, H. Eisaki, S. I. Uchida, K. Takegahara, H. Harima, Y. Saitoh, I. A. Nekrasov, G. Keller, D. E. Kondakov, A. V. Kozhevnikov, T. Pruschke, K. Held, D. Vollhardt, and V. I. Anisimov, Mutual experimental and theoretical validation of bulk photoemission spectra of $\text{Sr}_{1-x}\text{Ca}_x\text{VO}_3$, *Phys. Rev. Lett.* **93**, 156402 (2004).

[18] I. A. Nekrasov, G. Keller, D. E. Kondakov, A. V. Kozhevnikov, T. Pruschke, K. Held, D. Vollhardt, and V. I. Anisimov, Comparative study of correlation effects in CaVO_3 and SrVO_3 , *Phys. Rev. B* **72**, 155106 (2005).

[19] G. Ortiz and P. Ballone, Correlation energy, structure factor, radial distribution function, and momentum distribution of the spin-polarized uniform electron gas, *Phys. Rev. B* **50**, 1391 (1994).

[20] W. Nolting, W. Borgiel, V. Dose, and T. Fauster, Finite-temperature ferromagnetism of nickel, *Phys. Rev. B* **40**, 5015 (1989).

[21] W. Borgiel and W. Nolting, Many body contributions to the electronic structure of nickel, *Zeitschrift für Physik B Condensed Matter* **78**, 241 (1990).

[22] G. Ortiz and P. Ballone, Erratum: Correlation energy, structure factor, radial distribution function, and momentum distribution of the spin-polarized uniform electron gas [phys. rev. b 50, 1391 (1994)], *Phys. Rev. B* **56**, 9970 (1997).

[23] G. Giuliani and G. Vignale, *Quantum Theory of the Electron Liquid* (Cambridge University Press, 2005).

[24] K. Chen and K. Haule, A combined variational and diagrammatic quantum monte carlo approach to the many-electron problem, *Nature Communications* **10**, 3725 (2019).

[25] M. Holzmann, B. Bernu, C. Pierleoni, J. McMinis, D. M. Ceperley, V. Olevano, and L. Delle Site, Momentum distribution of the homogeneous electron gas, *Phys. Rev. Lett.* **107**, 110402 (2011).

[26] J. P. Perdew, K. Burke, and M. Ernzerhof, Generalized gradient approximation made simple, *Phys. Rev. Lett.* **77**, 3865 (1996).

[27] G. Cassabois, P. Valvin, and B. Gil, Hexagonal boron nitride is an indirect bandgap semiconductor, *Nature Photonics* **10**, 262 (2016).

[28] P. Gori-Giorgi, F. Sacchetti, and G. B. Bachelet, Analytic static structure factors and pair-correlation functions for the unpolarized homogeneous electron gas, *Phys. Rev. B* **61**, 7353 (2000).